Type of contribution:
Editorial
▶ Research Paper
Case Study
Review Paper
Scientific Data
Report of Tech. Application

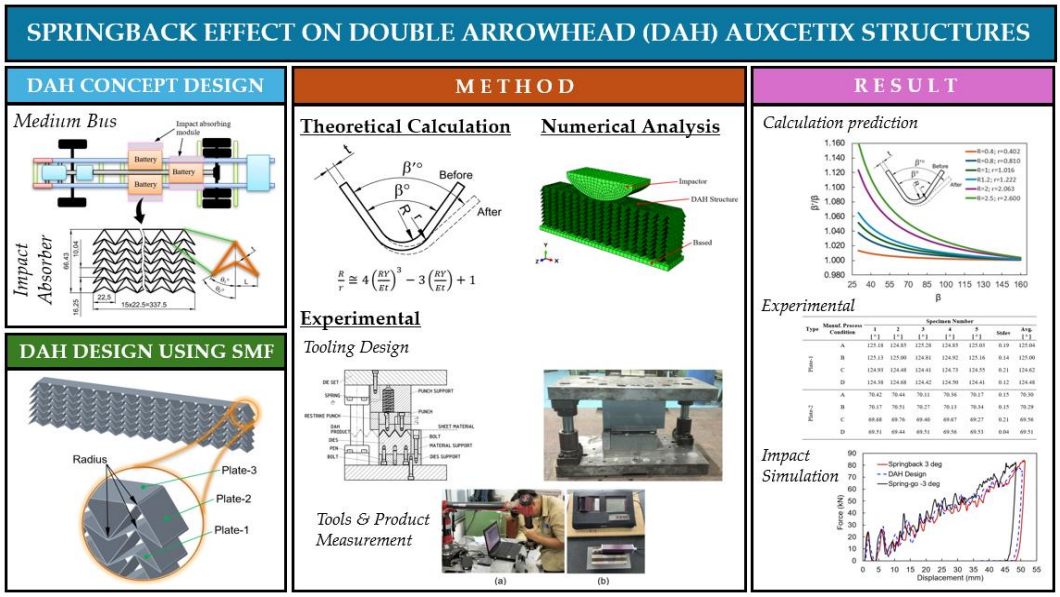
e-issn. 2798-5245

Mechanical Engineering for Society and Industry
Vol. 6, No. 1 (2026) pp 255-270
https://doi.org/10.31603/mesi.14655

Spring-back effect on double arrowhead auxetic structures for EV battery compartment protectors

Asep Indra Komara[1,2], Indrawanto[3]*, Rachman Setiawan[3], Bagus Budiwantoro[3], Dedy Ariefijanto[4]

[1] Doctoral Program of Mechanical Engineering, Faculty of Mechanical and Aerospace Engineering, Institut Teknologi Bandung, Bandung 40132, **Indonesia**
[2] Manufacturing Design Engineering Department, Politeknik Manufaktur Bandung, Bandung 40135, **Indonesia**
[3] Faculty of Mechanical and Aerospace Engineering, Institut Teknologi Bandung, Bandung 40132, **Indonesia**
[4] Manufacturing Engineering Department, Politeknik Manufaktur Bandung, Bandung 40135, **Indonesia**
✉ indrawanto@itb.ac.id



Highlights:

- DAH auxetic structures show promise as lightweight EV battery impact protectors.
- Manufacturing-induced spring-back affects the geometry and energy absorption of DAH.
- Punch-speed optimization and tooling compensation minimize spring-back defects.
- Experimental spring-back correction factors (Kθ) ranged from 1.002 to 1.025.

Abstract

Cellular structures such as double arrowhead (DAH) have great potential for development as impact-absorbing modules for electric-vehicle battery compartments. The DAH structure is relatively light and absorbs energy well, but the complex manufacturing presents challenges. One potential manufacturing process is sheet metal forming (SMF) technology. In SMF, a common obstacle is spring-back, which affects the assembly process and may reduce the energy-absorption performance of the DAH structure. This article aims to determine the effect of the manufacturing process on the spring-back of the DAH structure on its energy absorption performance. Experimental results showed that all tested conditions produced positive spring-back. Punch velocity had a greater influence than lubrication, where higher punch velocity reduced the spring-back angle, while lubrication showed only a minor effect. The experimental spring-back correction factor (K_θ) ranged from 1.002 to 1.025 depending on the forming conditions. These results indicate that spring-back can be effectively controlled by adjusting punch speed and compensating for tooling angle.

Keywords: Cellular structures; Double arrowhead; Impact absorber; Sheet metal; Spring-back

Article info
Submitted: 2025-08-28
Revised: 2026-05-18
Accepted: 2026-05-27

This work is licensed under a Creative Commons Attribution-NonCommercial 4.0 International License

Publisher
Universitas Muhammadiyah Magelang

Nomenclature			
ANOVA	Analysis of Variance	θ_1	Half of the bending angle of plate-1
ASTM	American Society for Testing and Materials	θ_2	Half of the bending angle of plate-2
CAD	Computer-Aided Design	β	Bending angle before the punch is released
CFE	Crush Force Efficiency	β'	Bending angle after the punch is released
CMM	Coordinate Measuring Machine	$\Delta\beta$	Spring-back angle
CNC	Computer Numerical Control	R_i	Radius before punch release
DAH	Double Arrowhead	R_f	Radius after punch release
DFM	design for manufacturing	β_1	Bend angle before punch is released from plate-1
EA	Energy Absorption	β_2	Bend angle before punch is released from plate-2
EDM	Electrical Discharge Machining	R_n	Neutral axis radius before the punch is released
EV	Electric Vehicle	r_n	Neutral axis radius after the punch is released
FEA	Finite Element Analysis	O_1	Center radius before the punch is released
ISO	International Organization for Standardization	O_2	Center radius after the punch is released
NSGA-II	Non-Dominated Sorting Genetic Algorithm II	$\widehat{AB}$	Neutral axis arc length before the punch is released
OES	Optical Emission Spectroscopy	$\widehat{AB}'$	Neutral axis arc length after the punch is released
POLMAN	Politeknik Manufaktur Bandung	α	The angle opposite to β before the punch release
SPM	Strokes per Minute	α'	The angle opposite to β' after the punch release
SEA	Specific Energy Absorption	R/r	Ratio of R to r
SMF	Sheet Metal Forming	R/t	Ratio of R to r
STDEV	Deviation Standard	A	velocity 6 mm/s, without lubrication
L	Width of half unit cell	B	velocity 6 mm/s, with lubrication
t	Plate thickness	C	velocity 180 mm/s, with lubrication
Y	Yield strength	D	velocity 180 mm/s, with lubrication
E	Young's modulus	K_θ	The spring-back factor was defined
K	Work hardening coefficient	ν	Poisson's ratio
n	Work hardening exponent	ε_0	plastic deformation

1. Introduction

Cellular structures were introduced by Gibson almost three decades ago at [1]. Cellular structures, such as wood, sponge, cancellous bone, and cork, are widely found in nature, as in [1], [2], [3], [4], [5]. Cellular structures possess mechanical, thermal, and acoustic properties that offer potential applications in various fields such as [6], [7], [8], [9]. Researchers from multiple fields, such as the aerospace industry, biomedical applications, body armor, thermal protection systems, heat exchanger systems, protective devices, soft robotics applications, footwear industry applications, cell growth substrates, vehicles, national defense, and mechanical parts, have developed various applications of cellular structures as one of the impact resistance technology solutions at [10], [11], [12]. Due to its complexity, manufacturing cellular structures remains a significant challenge.

Auxetic cellular structures, particularly the double arrowhead (DAH) configuration, have attracted increasing attention due to their negative Poisson's ratio and superior energy absorption capability, as in [13], making them promising candidates for impact protection in electric vehicle (EV) battery compartments. Recent studies have demonstrated that DAH structures can significantly enhance crashworthiness performance by enabling more effective energy dissipation. However, most existing research primarily focuses on geometric optimization, material selection, and impact behavior, while manufacturing aspects, especially those related to sheet metal forming (SMF), remain relatively underexplored.

In practical manufacturing using SMF processes, spring-back is an unavoidable phenomenon that can lead to geometric deviations from the intended design. Spring-back occurs in bent objects, in which the shape and dimensions of the deformed object change after bending due to residual stresses and elastic recovery [14], [15], [16]. These deviations may alter the cell topology, contact initiation, and load-transfer mechanisms, thereby affecting the peak force and overall energy-

absorption performance of the structure. Despite the growing number of studies on DAH structures [17]. The influence of spring-back on dimensional accuracy and its subsequent impact on crashworthiness has not been sufficiently investigated. This gap becomes particularly critical when considering the strict dimensional tolerances required for EV battery protection systems.

Therefore, this study aims to systematically investigate the effect of spring-back in the forming process of DAH auxetic structures, with particular emphasis on its influence on geometric accuracy and mechanical performance under impact loading. The study integrates experimental characterization, analytical evaluation, and numerical simulation to quantify spring-back-induced deviations and their correlation with key performance indicators, such as peak force and energy absorption.

The main contribution of this work lies in bridging the gap between manufacturability and crashworthiness of auxetic cellular structures by explicitly incorporating spring-back effects into the design–performance evaluation framework. Unlike previous studies that assume ideal geometry, this research provides a more realistic assessment by linking forming-induced deviations to structural performance. The novelty of this study lies in establishing a direct relationship between spring-back-induced geometric variation and impact energy absorption behavior in DAH structures, offering new insights for the design of manufacturable and reliable EV battery protection systems.

2. Methods

2.1. Material Properties of AA1050

The material chosen for the DAH structure is aluminum because of its lightweight properties. The composition of the aluminum material is characterized by optical emission spectroscopy (OES), as shown in **Table 1**. The mechanical properties of the aluminum material were determined by conducting tensile tests in accordance with ASTM E8. The Specimen, engineering, and actual stress-strain graphs for the aluminum sheet material from the tensile test are shown in **Figure 1**. Specimens were prepared from sheet metal manufactured with a laser cutting machine in accordance with ASTM E8. The tensile tests were conducted using a Zwick/Roell Z250 (type 8594) universal testing machine with a maximum load capacity of 250 kN. The machine was equipped with an Xforce P load cell (sensitivity: 2 mV/V). The crosshead speed was set to 0.015 mm/mm/min of the original gauge length, in accordance with ASTM E8. The elastic modulus was determined from the initial linear region of the stress–strain curve obtained from the tensile test data, where the elongation data were treated as engineering strain, and the applied load was converted into engineering stress (MPa). A linear regression was performed on the most linear portion within the elastic region, and the slope of the fitted line ($d\sigma/d\varepsilon$) yielded an elastic modulus of approximately 29.8 GPa. This value is significantly lower than the typical Young's modulus of AA1050-O (~69 GPa), primarily due to the use of crosshead displacement to represent elongation rather than local strain measured by an extensometer. The Young's modulus values are usually only 30% to 50% of the values obtained from quasi-static experiments [18]. Therefore, the reported value should be interpreted as an experimental (apparent) elastic modulus, rather than the intrinsic material property. The experimental results from several specimens indicate an average yield strength of 117 N/mm², calculated by dividing the force at the 0.2% strain offset (obtained from the tensile testing machine) by the specimen's cross-sectional area at the onset of permanent plastic deformation. Thus, due to the discrepancy in the elastic modulus obtained from the tensile test results, the elastic modulus value reported by Rusu [19] was adopted, as it exhibits yield characteristics similar to those of the material used in this study. Accordingly, an elastic modulus of 69,460 MPa was applied in the analysis.

Table 1. Chemical composition of AA1050

No	Element		Wt. %
1	Silicon	(Si)	0.097
2	Ferro	(Fe)	0.351
3	Copper	(Cu)	0.097
4	Manganese	(Mn)	0.007
5	Magnesium	(Mg)	0.002
6	Zinc	(Zn)	0.0008
7	Titanium	(Ti)	0.015
8	Chromium	(Cr)	0.002
9	Nickel	(Ni)	0.0008
10	Tin	(Sn)	0.0018
11	Natrium	(Na)	0.0004
12	Aluminum	(Al)	99.428

2.2. Design and Manufacture of the Cellular Structure

2.2.1. Cellular structure concept design

The design concept for the impact absorber using the DAH structure to be developed for the battery protection system is illustrated in **Figure 2**. The protective structure is placed on the outside

of the compartment. The dimensions of the DAH concept structure were obtained via optimization with the Non-Dominated Sorting Genetic Algorithm II (NSGA-II), using a fitness function derived from a third-order polynomial regression of the finite-element results, as described in Dharma and Setiawan, as in [20]. Several important dimensions of the DAH structure are θ_1 = 61.1°, θ_2 = 34.7°, L = 11.25 mm, and t = 1 mm. Next, the design concept is developed based on the characteristics of sheet metal. To obtain the energy absorption characteristics and assess the effectiveness of battery compartment protection, precise product test results are required to meet design specifications.

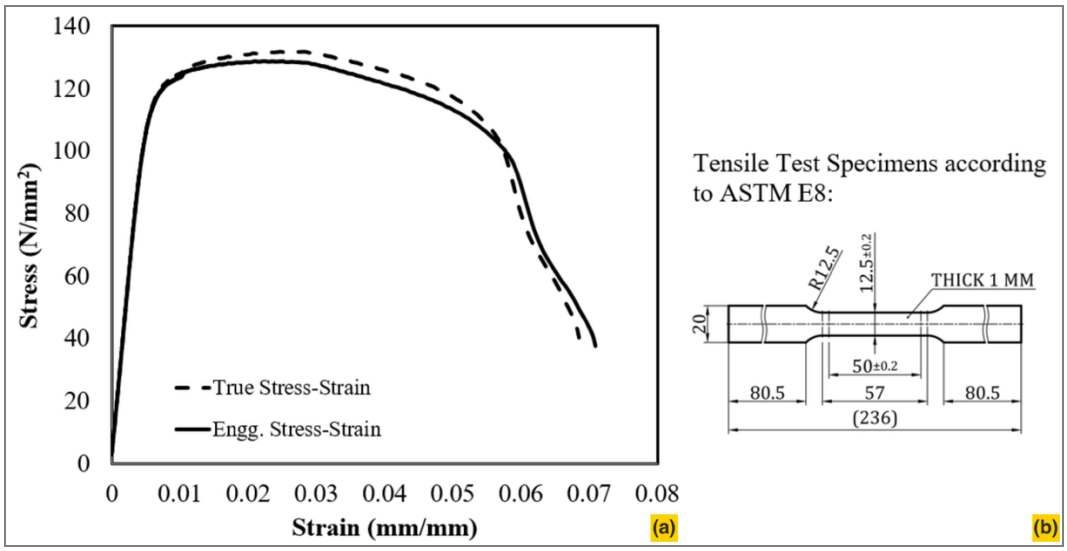


Figure 1. Aluminum sheet tensile test: (a) Engineering and True stress-strain transverse direction (b) Specimen geometric and dimension

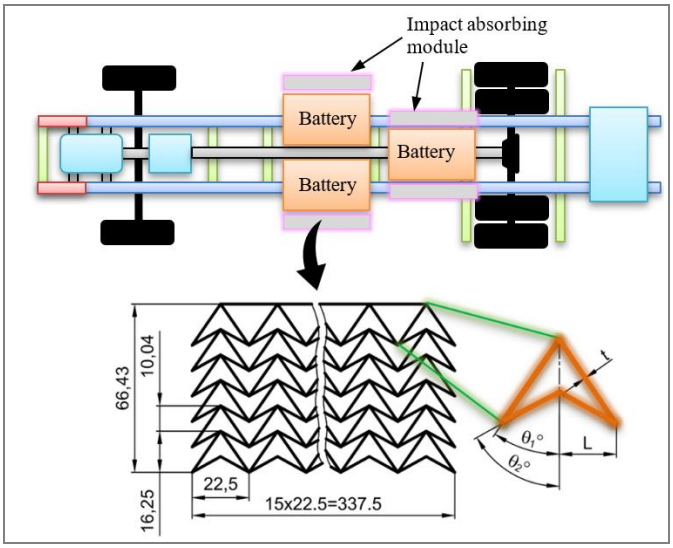


Figure 2. Design concept of DAH structures

Considering design for manufacturing (DFM), the DAH structural design concept was further developed into an impact-absorbing module to be manufactured using sheet metal technology. Several dimensions were adjusted to the manufacturing process, including adding a radius to the DAH cell unit. A radius must be provided due to the sheet metal forming process. The DAH structural design for sheet metal can be seen in **Figure 3**. The DAH structure consists of plates 1, 2, and 3. The next important consideration is how the dimensional parameters can be achieved during the manufacture of the DAH using SMF technology.

2.2.2. Tooling design, manufacturing, and measurement processes

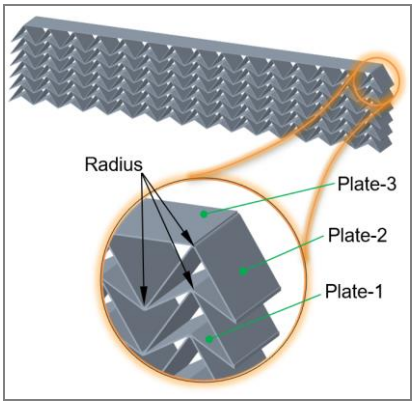


Figure 3. Design of DAH structures using sheet metal

A series of preparatory processes must be completed before the DAH structure is manufactured, including the design and manufacture of the forming tools, dimensional inspection of the punch and die components, and the subsequent manufacturing and metrological evaluation of the DAH structure.

The first step is to design the tool according to the specified specifications to get the appropriate arrowhead shape. The tooling design is illustrated in **Figure 4**. Tooling design consists of two sets of parts: a fixed side and a moving side. The main components of the tooling are punches and dies, which serve as sheet formers.

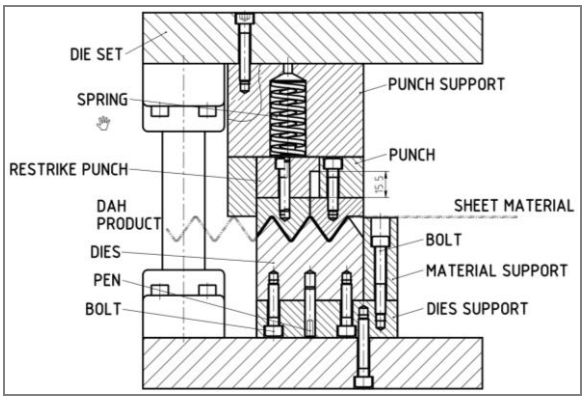


Figure 4. Tooling design for the DAH components

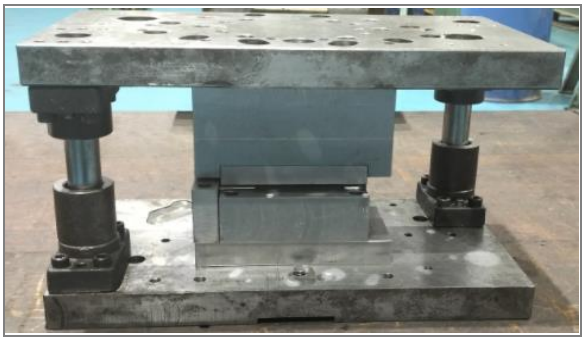


Figure 5. Press tool for DAH

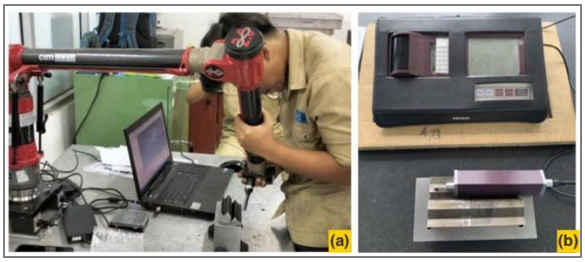


Figure 6. Punch and dies measurement: (a) Coordinate measuring machine; (b) Surface roughness testing

The designed tooling was subsequently manufactured using conventional and advanced machine tools. The machining processes employed included milling, turning, CNC milling, and wire-cut EDM. The manufactured tooling is presented in **Figure 5**.

The manufactured components of the DAH were then measured to determine any deviations and to verify whether they were within or outside the tolerance limits. Measurements were conducted at the Reverse Engineering and Prototyping Laboratory of the Manufacturing Design Engineering Department, POLMAN Bandung. Dimensional measurements of punches and dies are carried out using a Coordinate Measuring Machine (CMM), while roughness is measured using a surface roughness testing machine, as shown in **Figure 6a** and **Figure 6b**, respectively. The dimensions of the manufactured punches and dies adhere to the design and fall within the tolerance limits specified in ISO 2768-1. In addition, it is necessary to ensure that the surface roughness of the punch and dies is class N8, with Ra values between 1.6 µm and 3.2 µm.

2.2.3. Prototype and measurement

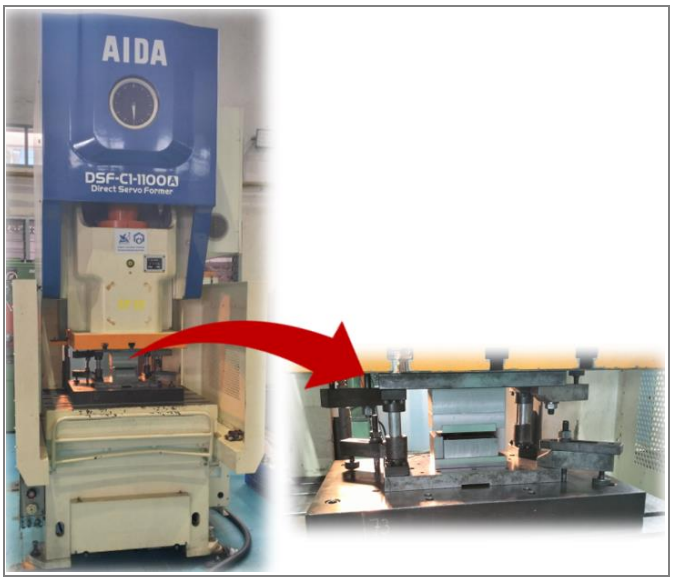


Figure 7. DAH tooling setup on the AIDA press machine

DAH manufacturing is carried out using an AIDA press machine, type DSF-C1-1100A Direct Servo Former, with a pressing capacity of 1100 kN and a maximum stroke rate of 70 strokes per minute. Several factors must be carefully considered during tool setup and the DAH manufacturing process, as shown in **Figure 7**. Several setup parameters to consider include punch strokes per minute (SPM), punch stroke length, maximum downward stroke, coaxial alignment between the punch and the dies, and parallelism between the punch and the dies. A feeler gauge is used to ensure a uniform 1 mm gap between the punch and the die. A trial using the actual material was performed to check whether the gap is in accordance with the design. The V-bending process was performed under two different speed conditions, and with or without lubrication on the punch and die, which is regulated as follows:

A = 1 SPM (velocity 6 mm/s), without lubrication;
B = 1 SPM (velocity 6 mm/s), with lubrication;
C = 30 SPM (velocity 180 mm/s), without lubrication, and;
D = 30 SPM (velocity 180 mm/s), with lubrication.

Punch speeds were set at 1 SPM and 30 SPM using the built-in control system of the AIDA 110-ton press. No external calibration or independent verification of the stroke rates was performed; therefore, the reported values represent the machine's nominal settings. This approach reflects common industry practice, although slight deviations between nominal and actual speeds were observed after time and motion studies.

The spring-back (Δβ) is measured from the difference between the bending angle of the product after the punch is released (β′) and the bending angle of the product before the punch is released (β), such that Δβ = β′ − β. Angle measurements were performed using an articulated arm CMM for the punch and die, and a gantry CMM for the DAH product. For each measured surface, six points were acquired: two on the right side, two on the left side, and two at the center of the specimen. The articulated arm CMM has an accuracy of 7 µm and a precision of 19 µm, while the gantry CMM provides an accuracy of 1 µm and a precision of 3 µm.

2.3. Theoretical Analysis of Spring-back Effect

Theoretical analysis of spring-back is conducted to obtain a big-picture view based on the mathematical model developed by Gardiner, which is simplified as in Gardiner, as in [21], as shown in Eq. (1). The Gardiner equation is one of the most widely used analytical approaches, as it was specifically developed to bridge the gap between pure elasticity theory and plastic deformation in bending processes. It is often considered more reliable for simple V-bending cases because it explicitly accounts for the ratio between yield strength (Y) and material stiffness (E). For AA1050, which exhibits relatively low yield strength but significant elasticity, the Y/E ratio is critical in determining the transition from permanent deformation to elastic recovery. Unlike models that assume the entire cross-section becomes fully plastic instantaneously, the Gardiner formulation adopts an elastic–perfectly plastic assumption. In simple V-bending, an "elastic core" exists around the neutral axis that never reaches the yield limit. This core acts as the primary spring element responsible for spring-back. The Gardiner equation mathematically incorporates the presence of this elastic core through a cubic term, making it more accurate than simple linear models. However, the model has several fundamental limitations, particularly for AA1050. It assumes elastic–perfectly plastic behavior without accounting for work hardening, thereby neglecting the increase in stress in the outer regions of the material. This leads to an underestimation of the internal bending moment and, consequently, an underprediction of spring-back compared to experimental results. Additional limitations include neglecting friction effects, assuming the cross-section remains plane, and omitting nonlinear unloading behavior. In addition, there is a theoretical model developed by Hasford and used by Salem for V-bending. Simple bending forms can usually be predicted accurately using theoretical equations, except for complex 3D bending forms. An illustration of V-bending is shown in **Figure 8**.

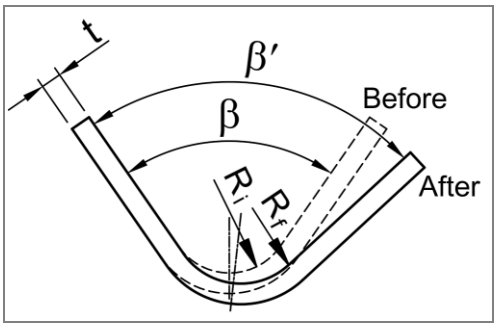


Figure 8. Illustration of spring-back in a simple bending case [22]

The equation developed by Gardiner:

$$\frac{R_i}{R_f} \cong 4\left(\frac{R_i Y}{Et}\right)^3 - 3\left(\frac{R_i Y}{Et}\right) + 1 \quad (1)$$

Where *E* is the material's Young's modulus, *Y* is the yield stress, *t* is the sheet thickness, β is the angle before the punch is removed, and β′ is the angle after the punch is removed. Spring-back is obtained as the difference between the punch angle (the expected angle) and the angle after the punch is removed from the sheet metal: $\Delta\beta = \beta' - \beta$. The above equation works reasonably well for a simple bending case and provides first-order insights into the magnitude of spring-back in terms of basic material properties. Some theoretical formulations to determine the spring-back factor (r) with the ratio of the radius of curvature before the punch is released (R_i) and after the punch is released (R_f), as stated by the Hasford and Cadell model [23], as in Eqs. (2) and (3).

$$r = \frac{1}{R_i} - \frac{1}{R_f} = \frac{6K'^{(1-\upsilon^2)}}{(n+2)\ t\ x\ E}\left(\frac{t}{2R_i}\right)^n \quad (2)$$

with

$$K' = K\left(\frac{4}{3}\right)^{\frac{n+1}{2}} \tag{3}$$

Salem also developed another model, [24] which is also defined by the ratio of the radii of curvature and accounts for the parameters (K, n) of the material's plastic behavior using Swift's law as in Eq. (4)

$$r = \frac{R_i}{R_f} = 1 - \frac{3K(1-v^2)}{(2+n)\,E\,\left(\frac{3}{4}\right)^{\frac{1+n}{2}}}\left(\frac{2R_i}{t}\right)^{1-n} \tag{4}$$

2.4. Numerical Simulation Method

This numerical simulation was conducted to predict the energy absorption characteristics of the DAH structure. Currently, many researchers conduct studies through numerical simulations to obtain an overview of product performance, such as in [25], [26], [27], [28]. Performance simulations were conducted to assess the sensitivity of the DAH geometry to ±3° angular deviations caused by spring-back in plates 1 and 2. The simulation process must consider several key factors, including CAD/FEA models, the number and type of meshing, and the appropriate boundary conditions. Numerical simulations are performed using the Abaqus application, as performed in [8], [29]. Numerical simulations were performed using a simplified FEA model by eliminating corner radii; a uniform thickness was assumed, and local thickness variations and thinning effects induced by manufacturing were not represented, as illustrated in **Figure 9**. Finite element models are created using a 3D shell-type model with a single structural unit to ensure good contact. At the same time, the material is assumed to exhibit isotropic behavior, thereby neglecting anisotropic effects. The impactor and base are modeled in 3D as discrete rigid bodies with a mass of 134 kg and an impact velocity of 5425 mm/s. All interactions are set using general contact (explicit) with the contact domain "included surface pairs all with self". After the convergence test process, it was decided to use a mesh size of 2.7 mm.

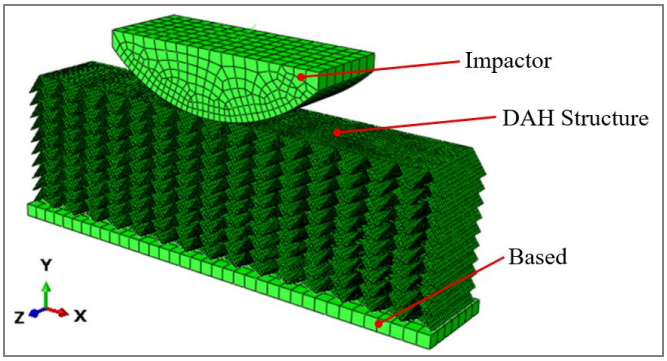


Figure 9. FEA model for impact simulation

2.5. Experimental Validation Process

The validation process begins with designing and manufacturing the tool, followed by creating a prototype of the DAH structure product using the press tool and press machine. The press used is an AIDA DSF-C1-1100A model, capable of applying a maximum force of 1100 kN. The main components of the press tool and the bending result of the DAH structure are then measured using a Coordinate Measuring Machine (CMM). The two main components, punches and dies, are measured to determine their radius, angular dimensions, and surface roughness, ensuring compliance with design specifications.

3. Results and Discussion

3.1. Theoretical Analysis Result

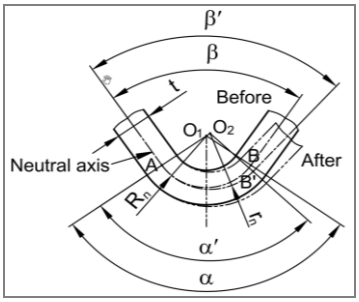


Figure 10. Spring-back assumption

The plate for DAH was bent with a radius equal to its thickness. Plate-1 is bent at an angle β_1= 122.2° ($2\theta_1$), and Plate-2 is bent at an angle β_2 = 69.4° ($2\theta_2$). In the bending process, the neutral axis of the plate is assumed not to change, where the elongation is zero [30], [31]. An illustration of the bending condition can be seen in **Figure 10**. Where O_1 is the center radius before bending, and O2 is the center radius after bending. R_n is the neutral axis radius before bending, and r_n is the neutral axis radius after bending. In contrast, is the angle opposite to angle

β before bending, and α′ is the angle opposite to β′ after bending. So $\alpha = 180° - \beta$ and $\alpha' = 180° - \beta'$. $\widehat{AB}$ and $\widehat{AB}'$ are neutral axes of the bending material, so they have the same length.

$$\widehat{AB} = 2\pi R_n \frac{\alpha}{360°} \tag{5}$$

$$\widehat{AB}' = 2\pi r_n \frac{\alpha'}{360°} \tag{6}$$

$$\beta' = 180° \left(1 - \frac{R_i + \frac{t}{2}}{R_f + \frac{t}{2}}\right) + \beta \left(\frac{R_i + \frac{t}{2}}{R_f + \frac{t}{2}}\right) \tag{7}$$

Based on Eqs. (1) and (4), the bending radius after the bending process and spring-back angle for some thickness and radius can be predicted as shown in **Table 2**. This spring-back estimation assumes that the arc length at the plate's neutral radius is the same before and after the effect of spring-back. Based on the theoretical estimation results in **Table 2**, The spring-back that occurs for the same R_i/R_f or R/t ratio will produce the same amount of spring-back. For example, at thicknesses of 0.8, 1.0, and 1.2 mm with the same R_i/R_f ratio of 0.995, Gardiner, Hasford, and Salem predict that spring-back will be constant at 0.38, 0.33, and 0.68, respectively. Spring-back predictions for DAH structural parameters, which are also listed in **Table 2**, are then compared with experimental results.

Table 2. Theoretical spring-back prediction for some different thicknesses and radii

t	R_i	β	Gardiner			Hasford			Salem		
[mm]	[mm]	[°]	R_i/R_f	β' [°]	Δβ [°]	R_i/R_f	β' [°]	Δβ [°]	R_i/R_f	β' [°]	Δβ [°]
0.8	0.8	69.38	0.995	69.755	0.375	0.996	69.708	0.328	0.991	70.037	0.657
0.8	1.2	69.38	0.992	70.013	0.633	0.993	69.923	0.543	0.987	70.469	1.089
0.8	1.6	69.38	0.990	70.281	0.901	0.991	70.143	0.763	0.983	70.908	1.528
1.0	0.8	69.38	0.996	69.657	0.277	0.996	69.625	0.245	0.993	69.870	0.490
1.0	1.0	69.38	0.995	69.755	0.375	0.996	69.708	0.328	0.991	70.037	0.657
1.0	2.0	69.38	0.990	70.281	0.901	0.991	70.143	0.763	0.983	70.908	1.528
1.2	0.6	69.38	0.997	69.521	0.141	0.998	69.507	0.127	0.995	69.634	0.254
1.2	1.2	69.38	0.995	69.755	0.375	0.996	69.708	0.328	0.991	70.037	0.657
1.2	2.4	69.38	0.990	70.281	0.901	0.991	70.143	0.763	0.983	70.908	1.528
0.8	0.8	121.94	0.995	122.137	0.197	0.804	122.112	0.172	0.991	122.285	0.345
0.8	1.2	121.94	0.992	122.272	0.332	0.996	122.225	0.285	0.987	122.511	0.571
0.8	1.6	121.94	0.990	122.413	0.473	0.993	122.340	0.400	0.983	122.742	0.802
1.0	0.8	121.94	0.996	122.085	0.145	0.991	122.068	0.128	0.993	122.197	0.257
1.0	1.0	121.94	0.995	122.137	0.197	0.996	122.112	0.172	0.991	122.285	0.345
1.0	2.0	121.94	0.990	122.413	0.473	0.996	122.340	0.400	0.983	122.742	0.802
1.2	0.6	121.94	0.997	122.014	0.074	0.991	122.007	0.067	0.995	122.073	0.133
1.2	1.2	121.94	0.995	122.137	0.197	0.998	122.112	0.172	0.991	122.285	0.345
1.2	2.4	121.94	0.990	122.413	0.473	0.996	122.340	0.400	0.983	122.742	0.802

3.2. Tooling Manufacturing and DAH Structure Measurement Result

The machined punch and die angles (α) were subsequently measured to verify their conformity with the design specifications (Dim. Target), as presented in **Table 3**. The punch and die dimensions fall within the permissible tolerance limits according to ISO 2768-1. Surface roughness was measured to ensure that the punch and die surfaces were comparable, thereby minimizing variations in contact conditions during bending. Since surface roughness influences friction at the tool–sheet interface, this step enables a clearer assessment of lubrication's effect. All punches and dies exhibited similar roughness levels, ranging from N7 (1.6 µm) to N8 (3.2 µm), indicating that differences in spring-back are primarily governed by material behaviour and process parameters rather than surface condition. Although surface roughness may affect spring-back indirectly through friction, its influence is generally less significant than that of material properties and tool geometry.

Table 3. Punch and die geometric measurement result

No	Component	Dim. Target [°]	α [°]	Dim. Difference	Tol. (ISO 2768-1)	R [mm]	Surface Roughness Ra [µm]
1	Punch 1	122.2	121.943	- 0°15′	± 0°20′	0.876	2.16
2	Dies 1	122.2	122.215	+ 0°1′	± 0°20′	1.669	2.20
3	Punch 2	69.4	69.381	- 0°1′	± 0°30′	0.801	1.99
4	Dies 2	69.4	69.104	- 0°18′	± 0°30′	1.562	2.58

After the tooling manufacturing process, the next step is to fabricate the DAH structural specimens. The measurement results of 1 mm thick plate specimens with parameters as in A, B, C, and D are shown in **Table 4**.

The results of the manufacturing process for Plate-1 and Plate-2, which are the components of the DAH, are shown in **Figure 11a** and **Figure 11b**. The next step is to combine the plate-1 and plate-2 sheets, arranged into several layers (6 to 10 layers) to form an impact-absorbing module, as shown in **Figure 11c**.

Table 4. Bending angle measurement results at various speeds and lubricant usage

Type	Manuf. Process Condition	Specimen Number						
		1 [°]	2 [°]	3 [°]	4 [°]	5 [°]	Stdev	Avg. [°]
Plate-1	A	125.18	124.85	125.28	124.85	125.03	0.19	125.04
	B	125.13	125.00	124.81	124.92	125.16	0.14	125.00
	C	124.93	124.48	124.41	124.73	124.55	0.21	124.62
	D	124.38	124.68	124.42	124.50	124.41	0.12	124.48
Plate-2	A	70.42	70.44	70.11	70.36	70.17	0.15	70.30
	B	70.17	70.51	70.27	70.13	70.34	0.15	70.29
	C	69.68	69.76	69.40	69.67	69.27	0.21	69.56
	D	69.51	69.44	69.51	69.56	69.53	0.04	69.51

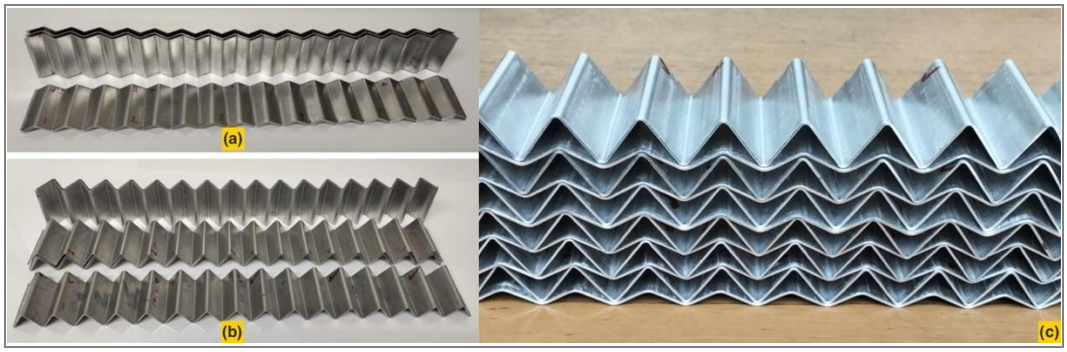


Figure 11. (a) DAH manufacturing component process result: Plate-1; (b) Plate-2; (c) Arrangement of DAH structural plates

3.3. Discussion

The primary challenge in the sheet-metal forming process is spring-back, which occurs when the forming force is removed from the workpiece. Various manufacturing process parameters can influence spring-back, including process conditions, bending techniques, punch/die profile geometry, material properties, and work material characteristics, as discussed in [32], [33], [34]. Spring-back induces dimensional variations in the Double Arrowhead (DAH) structures formed on plate-1 and plate-2. These discrepancies cause difficulties during assembly, particularly due to a mismatch in the DAH unit cell widths between the two plates. Based on Eq. (1), **Table 2** indicates that, although the R/t ratio remains constant, variations in the bending angle led to different spring-back responses. The effect of the R/t ratio on spring-back behavior is illustrated in **Figure 12**. Theoretically, an increase in the R/t ratio leads to a significant increase in spring-back. Experimentally, at a bending angle of 69.4°, the spring-back observed at a punch speed of 180 mm/s is close to the theoretical prediction. However, at a punch speed of 6 mm/s, the spring-back is significantly higher. Another trend is observed for plates with a larger bending angle (122°), where the experimental results deviate markedly from the theoretical predictions. This discrepancy is likely because the theoretical model does not account for friction effects, slight tool misalignment, and variations in the actual bending radius, punch-speed-dependent stress distribution, and neutral-axis shifting during the bending process. This condition is in line

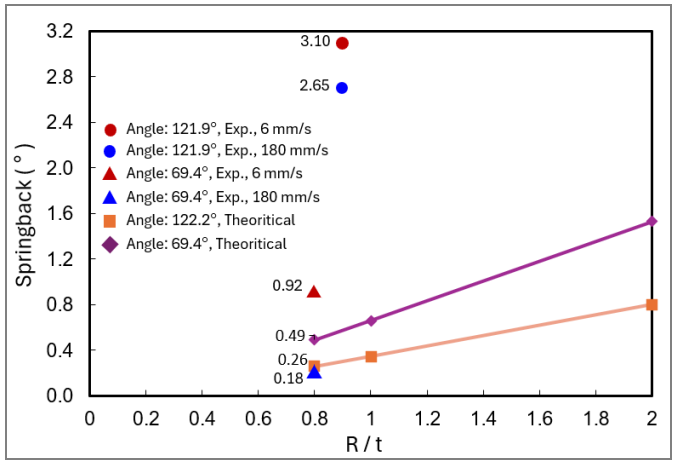


Figure 12. Effect of R/t ratio for some different angles based on Eq. (1) & experiment

with the results of numerical simulations and experiments conducted by Karakaya on [33], Thipprakmas [35] and M. Bakhshi-Jooybari [36].

During punch-and-die manufacturing, small deviations from the design dimensions may occur within tolerance limits, potentially affecting the final bending angle after unloading. A smaller punch angle tends to increase plastic deformation and spring-back, whereas a larger angle reduces them, as widely reported in the sheet metal forming literature [35]. Therefore, precise control of the tool angle is essential, particularly for DAH structures that are sensitive to geometric variations. Although this study did not experimentally evaluate the sensitivity of tool angle to spring-back, the relationship can be assessed analytically using Gardiner's equation, with linear regression and Pearson correlation to support the analysis. The results show an almost perfect negative linear correlation ($r \approx -1$, $p < 0.05$), indicating that decreasing the tool angle leads to a predictable increase in spring-back, with minimal experimental variability.

In practice, spring-back can be controlled through two primary approaches: increasing sheet tension and applying tooling-angle compensation, as in [37]. Tooling angle compensation is implemented using a spring-back correction factor (K_θ), as presented in **Table 5**. The geometric correction factor K_θ is defined as the ratio between the unloaded bending angle (after punch release) and the loaded bending angle (before punch release), i.e., $K_\theta = \beta'/\beta$. This correction factor is subsequently used to adjust the punch geometry to achieve the desired final product geometry.

The results indicate that Plate-1 exhibits significantly higher spring-back ($\Delta\beta \approx 2.54$–$3.10°$) than Plate-2 ($\Delta\beta \approx 0.13$–$0.92°$), suggesting greater sensitivity to geometric deviations. Increasing the punch speed from 6 mm/s to 180 mm/s consistently reduces spring-back in both plates, indicating that strain-rate effects promote plastic deformation and suppress elastic recovery. In contrast, lubrication shows a negligible influence, confirming that friction is a secondary factor. The analytical model predicts constant spring-back values, which deviate from experimental results, indicating its limitation in capturing real material behavior. The spring-back correction factor ($K_\theta > 1$) confirms the need for tool angle compensation, with higher values observed in Plate-1, implying greater adjustment requirements. Overall, spring-back is predominantly governed by tool geometry and punch speed, highlighting the importance of precise angle control and process parameter optimization, particularly for geometrically sensitive structures such as DAH.

Statistical analysis for Plate-1 and Plate-2 consistently showed that lubrication did not have a statistically significant effect on the spring-back effect under the tested conditions. For Plate-1, at a speed of 6 mm/s, ANOVA ($F = 0.106 < F_{crit} = 5.318$, $p = 0.753 > 0.05$) and independent t-test ($t = 0.326$, $p = 0.753 > 0.05$) showed no significant difference, while at a speed of 180 mm/s, ANOVA ($F = 0.904 < F_{crit} = 5.318$, $p = 0.370 > 0.05$) and Welch's t-test ($t = 0.951$, $p = 0.378 > 0.05$) also confirmed the absence of statistical significance. Similarly, for Plate-2, at a speed of 6 mm/s, ANOVA ($F = 0.01897$, $p = 0.894 > 0.05$) and independent t-test ($t = 0.138$, $p = 0.894 > 0.05$) showed no significant effect of lubrication, and at a speed of 180 mm/s, ANOVA ($F = 0.392$, $p = 0.549 > 0.05$) together with Welch's t-test ($t = 0.626$, $p = 0.559 > 0.05$) yielded the same conclusion. In all cases, the within-group variability exceeded the between-group differences, indicating that the observed variations were primarily influenced by experimental dispersion rather than the factors under study. Notably, the reduction in variance at higher pressing speeds and under lubrication conditions indicates improved process stability and more consistent bending behavior, although these improvements remained statistically insignificant.

Both Plate-1 and Plate-2 consistently demonstrate that punch speed has a statistically significant effect on spring-back under both lubricated and non-lubricated conditions. For Plate-1, under lubricated conditions, a significant difference is observed ($p = 0.000272 < 0.05$), indicating that increasing punch speed from 6 mm/s to 180 mm/s reduces spring-back. Under dry conditions,

Table 5. Spring-back factor for Plate-1 and Plate-2

Manuf. Process Condition	β [°]	β′ (Experiment) [°]	Δβ (Experiment) [°]	Spring-back Factor $K_\theta = \beta'/\beta$
Plate-1:				
6 mm/s, no lubrication	121.94	125.04	3.10	1.025
6 mm/s, with lubrication	121.94	125.00	3.06	1.025
180 mm/s, no lubrication	121.94	124.59	2.65	1.022
180 mm/s, with lubrication	121.94	124.48	2.54	1.021
Plate-2:				
6 mm/s, no lubrication	69.38	70.30	0.92	1.013
6 mm/s, with lubrication	69.38	70.29	0.91	1.013
180 mm/s, no lubrication	69.38	69.56	0.18	1.003
180 mm/s, with lubrication	69.38	69.51	0.13	1.002

the effect remains significant ($p = 0.0103 < 0.05$), although with a lower level of statistical strength, suggesting a moderate influence of punch speed. For Plate-2, the effect is even more pronounced. Under lubricated conditions, ANOVA ($F = 120.81$, $p = 4.17 \times 10^{-6} < 0.05$) and Welch t-test ($t = 10.99$, $p = 0.000108 < 0.05$) indicate a highly significant reduction in spring-back with increasing punch speed, accompanied by improved process stability as reflected by lower variance. Similarly, under dry conditions, a significant difference is observed ($p = 0.000207 < 0.05$), confirming that higher punch speed substantially reduces spring-back. This condition is in line with research by Choi et al. [38]. Overall, these results indicate that punch speed is a dominant parameter influencing spring-back behavior, with consistently lower spring-back values obtained at higher deformation speeds across all conditions.

The **Figure 13** presents bar charts with error bars for Plate-1 and Plate-2 under varying punch speeds and lubrication conditions. For Plate-1, the spring-back values are relatively high at 6 mm/s and decrease at 180 mm/s, while the difference between lubricated and non-lubricated conditions is minimal, with overlapping error bars indicating no significant effect of lubrication. In contrast, the consistent reduction from 6 mm/s to 180 mm/s highlights a clear influence of punch speed. A similar but more pronounced trend is observed for Plate-2, where spring-back decreases substantially at higher speed, accompanied by smaller error bars at 180 mm/s, suggesting improved process stability. The differences between lubricated and non-lubricated conditions remain minor compared to the effect of punch speed. Overall, this visualization is consistent with the statistical analysis, confirming that punch speed is the dominant factor significantly reducing spring-back, while lubrication does not have a statistically significant effect but tends to enhance process consistency.

The spring-back prediction based on Equation (1) for plate-1 shows a substantial deviation from the experimental results. This difference is attributed to inaccuracies in estimating the plate radius after bending, which is in agreement with the results reported by Yang et al. [14]. The significant discrepancy between the experimental results and theoretical predictions at a large bending angle (122.2°) is primarily due to the theoretical model's limitations, which assume linear-elastic behavior and an idealized stress distribution. Under large-deformation conditions, the effects of nonlinear unloading, neutral-axis shift, material anisotropy, and friction lead to greater spring-back than predicted by the theoretical model. One key factor is the assumption that the neutral axis remains fixed at the mid-thickness (t/2), whereas in reality it shifts toward the inner radius during bending, substantially altering the internal bending moment. The analytical formulation does not account for this shift. Moreover, the analytical model neglects nonlinear elastic unloading. In practice, upon load removal, the material does not follow a perfectly linear-elastic path because the effective elastic modulus degrades after plastic deformation. Eggertsen and Mattiasson reported that assuming a constant elastic modulus is a major source of error, leading to significant underestimation of spring-back in theoretical predictions, as in [39]. In addition, the model does not incorporate strain-hardening behavior, particularly kinematic hardening. As a result, the elastic energy stored during deformation is underestimated compared to actual experimental conditions. Chun et al. demonstrated that neglecting the Bauschinger effect leads to underprediction of spring-back [40]. Furthermore, friction at the punch–die–sheet interface influences the tensile stress distribution in the deformation zone. A higher friction coefficient tends to increase tensile stress in the sheet, which may reduce spring-back by shifting the neutral axis further and promoting a more plastic-dominated bending moment distribution. However, non-uniform friction can introduce surface defects and dimensional inconsistencies.

The theoretical predictions consistently indicate spring-back (**Table 2**), reaching up to +2.76° at an R/r ratio of 0.969, which is close to +3°. Meanwhile, based on previous studies [35], particularly in sheet metal forming (SMF) experiments, spring-go conditions may also occur.

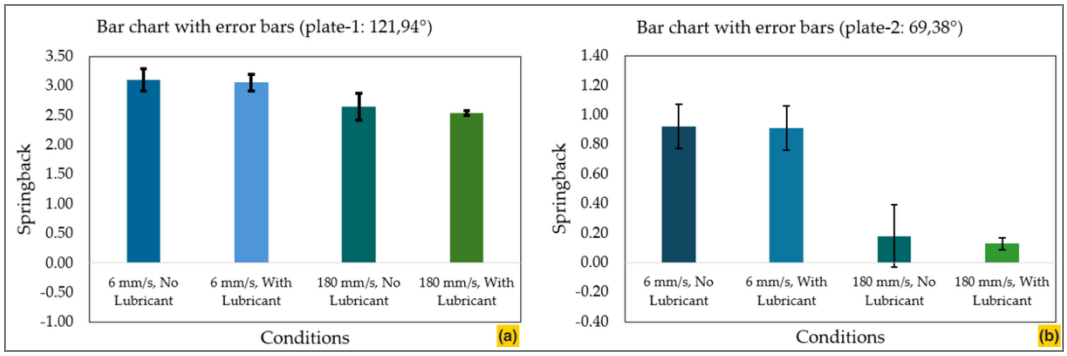


Figure 13. Bar chart with error bars for: (a) plate-1; (b) plate-2

Therefore, in the manufacturing process of the DAH structure, we investigated the impact energy absorption behavior under geometric deviations of +3° or -3°, as presented in **Table 6** and **Table 7**. In the SMF process, spring-go is most likely caused by the actual bending mechanism during the forming process. Based on previous studies, spring-go (negative spring-back) can occur when local reverse bending appears outside the main bending area. This creates a residual stress pattern opposite to normal spring-back. This phenomenon is strongly affected by tool geometry and contact conditions, such as punch tip radius, bending angle, sheet thickness, and the level of punch–die contact during forming. In V-bending, a small punch radius, excessive punch penetration, or full-contact conditions can create reverse bending near the sheet leg area. As a result, after unloading, the sheet may move forward instead of showing normal spring-back.

The potential for dimensional mismatch in the DAH structure due to spring-back/spring-go is then simulated using nonlinear explicit Abaqus to provide an overview of the DAH structure's impact energy absorption performance. The simulation results for the impact energy absorption of the DAH variations assembled based on plate-1 are presented in **Table 6**, and for the DAH structure assembled based on plate-2, is shown in **Table 7**. **Table 6** and **Table 7** shows the energy absorption characteristics of the DAH structure at the design target angle (spring-back = 0), with positive spring-back prediction up to +3°, and with negative spring-go prediction up to –3° by using numerical simulations.

The difference in energy absorption capacity due to spring-back or spring-go when assembled based on plate-1 results in a maximum performance reduction of 30 joules (1.53%), and when assembled based on plate-2, the maximum performance reduction is 35 joules (1.78%). This trend of decreasing energy absorption performance is not too significant for EV battery protection using AA1050 material. However, the difference in the geometric dimensions of the two plates due to spring-back will pose an obstacle during assembly into a DAH structure, where this product demands precision. Spring-back/spring-go variations have a stronger effect on peak force (F_{peak}) than on energy absorption (EA). F_{peak} shows wider variation, indicating high sensitivity to small geometric changes, especially during initial contact and collapse. In contrast, EA and SEA remain relatively stable across all cases. From a crashworthiness perspective, EA and SEA are more critical, as they represent the total absorbed energy and efficiency, respectively. The stable EA and SEA values indicate that the overall energy absorption capability of the DAH structure is not significantly affected by spring-back. Therefore, although spring-back influences F_{peak}, its impact on overall crashworthiness performance is limited, making EA and SEA more reliable indicators.

The simulation results indicate that variations in spring-back from -3 ° to +3° have a negligible effect on energy absorption (EA). The EA values remain within a narrow range of 1932–1962 J, corresponding to a variation of less than 2% relative to the nominal design. No clear monotonic trend is observed, suggesting that EA is relatively insensitive to geometric deviations induced by spring-back. This implies that although spring-back alters the geometry, it does not significantly affect the structure's overall energy-dissipation capability. Therefore, from a crashworthiness perspective, the DAH structure demonstrates robust energy-absorption performance in the presence of spring-back-induced geometric variations. Statistical significance analysis using ANOVA and t-tests also yields p-values > 0.05, indicating that the variation in EA is not statistically significant. On the other hand, geometric deviations in the DAH structure caused by spring-back can lead to assembly difficulties between the two components (Plate-1 and Plate-2). Therefore, this study focuses on mitigating spring-back.

Table 6. Effect of spring-back/spring-go on DAH performance for assembly based on plate-1

Spring-back / Spring-go [°]	β'_1 [°]	F_{Peak} [kN]	F_{Mean} [kN]	EA [Joule]	SEA [J/kg]	CFE
+3	125.2	84.04	37.76	1935	1106	0.45
+2.5	124.7	81.47	38.12	1939	1108	0.47
+2	124.2	84.21	38.38	1935	1106	0.46
+1.5	123.7	86.43	38.23	1935	1106	0.44
+1	123.2	85.26	38.61	1941	1109	0.45
+0.5	122.7	80.50	38.91	1948	1113	0.48
Design (0°)	122.2	77.72	38.89	1962	1121	0.50
-0.5	121.7	83.28	38.97	1932	1104	0.47
-1	121.2	81.85	39.28	1942	1110	0.48
-1.5	120.7	79.57	39.66	1948	1113	0.50
-2	120.2	81.82	39.75	1946	1112	0.49
-2.5	119.7	83.91	39.83	1945	1111	0.47
-3	119.2	82.40	40.22	1949	1114	0.49

Table 7. Effect of spring-back/spring-go on DAH performance for assembly based on plate-2

Spring-back / Spring-go [°]	β'_2 [°]	F_{Peak} [kN]	F_{Mean} [kN]	EA [Joule]	SEA [J/kg]	CFE
+3	66.4	76.64	36.41	1945	1112	0.48
+2.5	66.9	74.17	36.87	1948	1113	0.50
+2	67.4	78.61	37.74	1955	1117	0.48
+1.5	67.9	79.88	38.19	1945	1111	0.48
+1	68.4	79.55	40.18	1948	1113	0.51
+0.5	68.9	80.99	38.49	1934	1105	0.48
Design (0°)	69.4	77.72	38.89	1962	1121	0.50
-0.5	69.9	81.44	38.20	1942	1110	0.47
-1	70.4	83.24	39.77	1948	1113	0.48
-1.5	70.9	86.30	40.29	1939	1108	0.47
-2	71.4	78.85	40.88	1948	1113	0.52
-2.5	71.9	82.84	41.37	1941	1109	0.50
-3	72.4	86.79	41.85	1927	1101	0.48

Nevertheless, the force–displacement responses of Plate-1 and Plate-2 under geometric variations induced by spring-back (+3°) and spring-go (−3°) exhibit generally similar progressive crushing behavior compared to the baseline DAH design, as shown in **Figure 14**. In the early deformation stage (0–20 mm), all curves show comparable initial stiffness and force fluctuations, indicating that the onset of deformation and local buckling mechanisms are not significantly affected by the geometric deviations. In the next 20-40 mm deformation stages, the responses begin to diverge slightly. The spring-go (−3°) configurations, particularly for Plate-2, tend to exhibit higher force levels and more pronounced oscillations, suggesting earlier contact interaction and increased structural stiffness due to geometric tightening. In contrast, the spring-back (+3°) cases show relatively lower and smoother force evolution, indicating a slight reduction in stiffness and delayed contact initiation. At larger displacements (> 40 mm), the differences become more evident. The spring-go (−3°) cases reach higher peak forces earlier, while the spring-back (+3°) cases tend to shift the peak force toward larger displacements. However, despite these differences in peak force and deformation progression, the overall area under the curve (energy absorption) remains relatively similar across all cases. These results confirm that geometric variations due to spring-back primarily influence the force-response characteristics (e.g., peak force and deformation sequence) but have a limited effect on the total energy absorption capacity, which remains relatively stable across configurations.

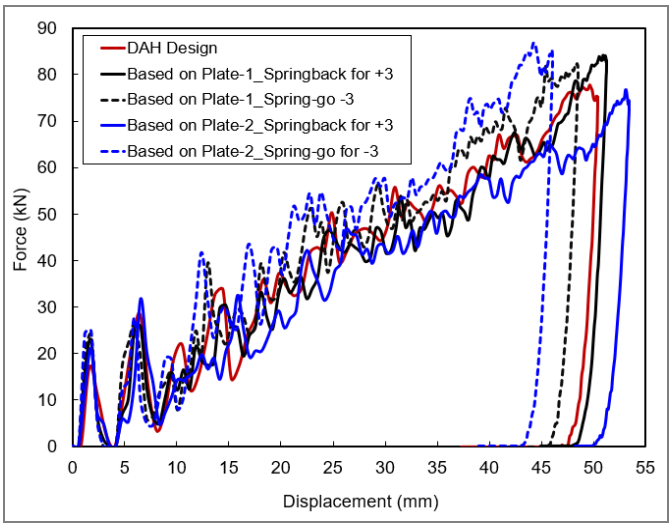


Figure 14. Load distribution against displacement when the DAH structure is given an impact load when assembled based on plate-1 and plate-2

4. Conclusion

This study presents a new investigation of spring-back behavior in auxetic Double Arrowhead (DAH) structures for electric vehicle (EV) battery protection. All experimental conditions exhibited positive spring-back, with magnitudes varying with punch speed and lubrication. Higher punch speed reduced spring-back, while lubrication had only a minor effect. Spring-go was not observed experimentally, but it was also evaluated as a possible geometric deviation to understand its potential influence on crashworthiness. The results show that spring-back control should primarily focus on selecting forming speed and compensating for the tooling angle using an appropriate correction factor. The comparison between theoretical and experimental results also indicates that simplified analytical models can predict the general trend, but may not fully represent the behavior of complex DAH geometries. These findings provide useful guidance for improving dimensional accuracy, assembly quality, and structural reliability of EV battery compartment components.

Future studies should examine the combined effects of sheet thickness, tool angle, DAH dimensions, lubrication, and other forming parameters, as well as impact energy absorption, to determine the optimal manufacturing conditions for high-performance, highly manufacturable DAH structures.

Authors' Declaration

Authors' contributions and responsibilities – The authors made substantial contributions to the study's conception and design. The authors took responsibility for data analysis, interpretation, and discussion of results. The authors read and approved the final manuscript.

Funding – No funding information from the authors.

Availability of data and materials – All data is available from the authors.

Competing interests – The authors declare no competing interests.

Additional information – No additional information from the authors.

References

[1] L. J. Gibson and M. F. Ashby, *Cellular solids, structure and properties*, 2nd Ed. Cambridge, United Kingdom: Cambridge University Press, 1997.

[2] L. J. Gibson, "Modelling the mechanical behavior of cellular materials," *Materials Science and Engineering: A*, vol. 110, no. C, pp. 1–36, Mar. 1989, doi: 10.1016/0921-5093(89)90154-8.

[3] C. O. Ufodike, M. F. Ahmed, and G. Dolzyk, "Additively manufactured biomorphic cellular structures inspired by wood microstructure," *Journal of the Mechanical Behavior of Biomedical Materials*, vol. 123, no. August 2021l, p. 104729, Nov. 2021, doi: 10.1016/j.jmbbm.2021.104729.

[4] L. J. Gibson, "Biomechanics of cellular solids," *Journal of Biomechanics*, vol. 38, no. 3, pp. 377–399, Mar. 2005, doi: 10.1016/j.jbiomech.2004.09.027.

[5] M. Mudassir, F. Tarlochan, and M. A. Mansour, "Nature-Inspired Cellular Structure Design for Electric Vehicle Battery Compartment: Application to Crashworthiness," *Applied Sciences*, vol. 10, no. 13, p. 4532, Jun. 2020, doi: 10.3390/app10134532.

[6] A. Evans, "Multifunctionality of cellular metal systems," *Progress in Materials Science*, vol. 43, no. 3, pp. 171–221, Jul. 1998, doi: 10.1016/S0079-6425(98)00004-8.

[7] Q. Feng, Q. Tang, Z. Liu, Y. Liu, and R. Setchi, "An investigation of the mechanical properties of metallic lattice structures fabricated using selective laser melting," *Proceedings of the Institution of Mechanical Engineers, Part B: Journal of Engineering Manufacture*, vol. 232, no. 10, pp. 1719–1730, Aug. 2018, doi: 10.1177/0954405416668924.

[8] Y. Zhao, Y. Wang, J. Hao, Y. Wang, K. Wang, and S. Tai, "Study on mechanical properties of cellular structures with negative Poisson's ratio based on the development of Abaqus plug-in tool," *Composite Structures*, vol. 322, no. July, p. 117348, Oct. 2023, doi: 10.1016/j.compstruct.2023.117348.

[9] A. Sur, S. Narkhede, and S. Darvekar, "Applications, Manufacturing and Thermal Characteristics of Micro-Lattice Structures: Current State of the Art," *Engineering Journal*, vol. 23, no. 6, pp. 419–431, Nov. 2019, doi: 10.4186/ej.2019.23.6.419.

[10] U. Sajjad, T. Rehman, M. Ali, C. W. Park, and W.-M. Yan, "Manufacturing and potential applications of lattice structures in thermal systems: A comprehensive review of recent advances," *International Journal of Heat and Mass Transfer*, vol. 198, p. 123352, Dec. 2022, doi: 10.1016/j.ijheatmasstransfer.2022.123352.

[11] M. Ali *et al.*, "On the assessment of the mechanical properties of additively manufactured lattice structures," *Engineering Analysis with Boundary Elements*, vol. 142, no. February, pp. 93–116, Sep. 2022, doi: 10.1016/j.enganabound.2022.05.019.

[12] H. Yin, W. Zhang, L. Zhu, F. Meng, J. Liu, and G. Wen, "Review on lattice structures for energy absorption properties," *Composite Structures*, vol. 304, no. October 2022, p. 116397, Jan. 2023, doi: 10.1016/j.compstruct.2022.116397.

[13] X. Xue, C. Lin, F. Wu, Z. Li, and J. Liao, "Lattice structures with negative Poisson's ratio: A

review," *Materials Today Communications*, vol. 34, no. 8 December 2022, p. 105132, Mar. 2023, doi: 10.1016/j.mtcomm.2022.105132.

[14] S. Yang, Y. Wen, H. Sun, C. Liang, and Y. Li, "Study on springback prediction based on neutral layer displacement in three-dimensional stretch-bending forming of profiles," *International Journal of Solids and Structures*, vol. 311, no. November 2024, p. 113241, Apr. 2025, doi: 10.1016/j.ijsolstr.2025.113241.

[15] C.-C. Chu, "The effect of restraining force on springback," *International Journal of Solids and Structures*, vol. 27, no. 8, pp. 1035–1046, 1991, doi: 10.1016/0020-7683(91)90099-2.

[16] L. Reddy, B. C. Rao, P. R. Reddy, and P. V. R. R. Reddy, "A Review on Springback in Metal Forming," *International Journal of Engineering Research & Technology*, vol. 3, no. 1, pp. 646–655, 2014.

[17] R. Setiawan, A. I. Komara, and B. Budiwantoro, "Numerical and experimental investigation of aluminum double arrowhead cellular structure manufactured using sheet metal forming," *Results in Engineering*, vol. 26, no. January, p. 104667, Jun. 2025, doi: 10.1016/j.rineng.2025.104667.

[18] G. Gray III and H. Kuhn, "Classic Split-Hopkinson Pressure Bar Testing," in *Mechanical Testing and Evaluation*, Materials Parks, Ohio: ASM International, 2000, pp. 462–476. doi: 10.31399/asm.hb.v08.a0003296.

[19] G.-P. Rusu, R.-E. Breaz, M.-O. Popp, V. Oleksik, and S.-G. Racz, "Experimental Research on Wolfram Inert Gas AA1050 Aluminum Alloy Tailor Welded Blanks Processed by Single Point Incremental Forming Process," *Materials*, vol. 16, no. 19, p. 6408, Sep. 2023, doi: 10.3390/ma16196408.

[20] I. G. S. S. Dharma and R. Setiawan, "Comparative Review of Multi-Objective Optimization Algorithms for Design and Safety Optimization in Electric Vehicles," *IEEE Access*, vol. 12, no. October, pp. 146376–146396, 2024, doi: 10.1109/ACCESS.2024.3475032.

[21] F. J. Gardiner, "The Spring Back of Metals," *Journal of Fluids Engineering*, vol. 79, no. 1, pp. 1–7, Jan. 1957, doi: 10.1115/1.4012908.

[22] A. Behrouzi, B. Mollaei Dariani, and M. Shakeri, "Tool shape design in V-bending and channel forming processes by inverse analysis of springback," *Inverse Problems in Science and Engineering*, vol. 18, no. 4, pp. 465–480, Jan. 2010, doi: 10.1080/17415971003624355.

[23] W. F. Hasford and M. F. Caddell, *Metal Forming Mechanics and Metallurgy*, THIRD EDIT. Cambridge: Cambridge University Press, 2007.

[24] C. Ben Salem and W. Meslameni, "A Numerical Investigation on the Springback in Air V-Banding of Aluminum 1050 A," *International Journal of Research in Industrial Engineering*, vol. 11, no. 2, pp. 119–133, 2022, doi: 10.22105/riej.2022.337535.1308.

[25] S. Sabari, D. G. Andrade, C. Leitão, F. Simões, and D. M. Rodrigues, "Influence of the strain hardening behaviour on the tensile and compressive response of aluminium auxetic structures," *Composite Structures*, vol. 305, no. October 2022, p. 116472, Feb. 2023, doi: 10.1016/j.compstruct.2022.116472.

[26] A. Mohan, P. Mondal, and J. Rengaswamy, "Impact behavior of auxetic structures: Experimental and numerical analysis," *Materials Today: Proceedings*, vol. 87, no. xxxx, pp. 292–298, 2023, doi: 10.1016/j.matpr.2023.05.631.

[27] M. Nasim, M. J. Hasan, and U. Galvanetto, "Impact behavior of energy absorbing helmet liners with PA12 lattice structures: A computational study," *International Journal of Mechanical Sciences*, vol. 233, no. August, p. 107673, Nov. 2022, doi: 10.1016/j.ijmecsci.2022.107673.

[28] B. Uspensky, I. Derevianko, K. Avramov, K. Maksymenko-Sheiko, and M. Chernobryvko, "Mechanical Properties of Auxetic Honeycombs Realized via Material Extrusion Additive Manufacturing: Experimental Testing and Numerical Studies," *Applied Composite Materials*, vol. 32, no. 1, pp. 119–148, Feb. 2025, doi: 10.1007/s10443-024-10269-2.

[29] A. D. Gudayu, L. Steuernagel, and D. Meiners, "The capability of ABAQUS/CAE to predict the tensile properties of sisal fiber reinforced polyethylene terephthalate composites," *Composites and Advanced Materials*, vol. 31, pp. 1–13, Jan. 2022, doi: 10.1177/26349833221137602.

[30] L. Vinet and A. Zhedanov, "A 'missing' family of classical orthogonal polynomials," *Journal of Physics A: Mathematical and Theoretical*, vol. 44, no. 8, p. 085201, Feb. 2011, doi:

10.1088/1751-8113/44/8/085201.

[31] T. Altan and A. E. Tekkaya, *Sheet Metal Forming: Processes and Applications*. ASM International, 2012. doi: 10.31399/asm.tb.smfpa.9781627083171.

[32] I. A. Choudhury and V. Ghomi, "Springback reduction of aluminum sheet in V-bending dies," *Proceedings of the Institution of Mechanical Engineers, Part B: Journal of Engineering Manufacture*, vol. 228, no. 8, pp. 917–926, Aug. 2014, doi: 10.1177/0954405413514225.

[33] Ç. Karakaya and S. Ekşi, "Springback Behavior of AA 7075-T6 Alloy in V-Shaped Bending," *Applied Sciences*, vol. 15, no. 10, p. 5509, May 2025, doi: 10.3390/app15105509.

[34] S. Tejyan, N. Kumar, R. Kant Ravi, V. Singh, and B. Gangil, "Analysis of spring back effect for AA6061 alloy sheet using finite element analysis," *Materials Today: Proceedings*, May 2024, doi: 10.1016/j.matpr.2024.05.122.

[35] S. Thipprakmas and W. Phanitwong, "Process parameter design of spring-back and spring-go in V-bending process using Taguchi technique," *Materials & Design*, vol. 32, no. 8–9, pp. 4430–4436, Sep. 2011, doi: 10.1016/j.matdes.2011.03.069.

[36] M. Bakhshi-Jooybari, B. Rahmani, V. Daeezadeh, and A. Gorji, "The study of spring-back of CK67 steel sheet in V-die and U-die bending processes," *Materials & Design*, vol. 30, no. 7, pp. 2410–2419, Aug. 2009, doi: 10.1016/j.matdes.2008.10.018.

[37] R. H. Wagoner, H. Lim, and M.-G. Lee, "Advanced Issues in springback," *International Journal of Plasticity*, vol. 45, pp. 3–20, Jun. 2013, doi: 10.1016/j.ijplas.2012.08.006.

[38] M. K. Choi and H. Huh, "Effect of Punch Speed on Amount of Springback in U-bending Process of Auto-body Steel Sheets," *Procedia Engineering*, vol. 81, no. October, pp. 963–968, 2014, doi: 10.1016/j.proeng.2014.10.125.

[39] P.-A. Eggertsen and K. Mattiasson, "On constitutive modeling for springback analysis," *International Journal of Mechanical Sciences*, vol. 52, no. 6, pp. 804–818, Jun. 2010, doi: 10.1016/j.ijmecsci.2010.01.008.

[40] B. K. Chun, J. T. Jinn, and J. K. Lee, "Modeling the Bauschinger effect for sheet metals, part I: theory," *International Journal of Plasticity*, vol. 18, no. 5–6, pp. 571–595, Oct. 2002, doi: 10.1016/S0749-6419(01)00046-8.